2017 IEEE International Conference on Robotics and Automation (ICRA)
Singapore, May 29 - June 3, 2017

Phase Control for a Legged Microrobot Operating at Resonance

Neel Doshi, Kaushik Jayaram, Benjamin Goldberg, and Robert J Wood

***Abstract*— We present an off-board phase estimator and controller for leg position near the resonance of the Harvard Ambulatory MicroRobot's (HAMR) two degree-of-freedom transmission. This control system is a first step towards leveraging the significant increase in stride length at transmission resonance for faster and more efficient locomotion. We experimentally characterize HAMR's transmission and determine that actuator phase is a sufficient proxy for leg phase across the range of useful operating frequencies (1-120Hz). An estimator is developed to determine actuator phase using off-board position sensors and it converges within a cycle on average. We also fit a nonlinear dynamic model of the transmission to the experimental data, and utilize the model to determine a suitable open-loop resonant leg trajectory and define feed forward control inputs. This resonant (100Hz) trajectory is theoretically 50% more efficient than pre-resonant high speed running trajectories. The controller converges to this trajectory in 0.05 ± 0.02 seconds (5.3 ± 2.4 cycles) in air, and in 0.05 ± 0.01 seconds (4.7 ± 0.6 cycles) under perturbations that approximate ground contact.**

***Index Terms*— Resonance, Phase control, Dynamic modeling, Legged microrobots, Biologically Inspired Robots**

I. Introduction

Several biological and engineered systems exploit the benefits of resonance, including low input impedance, high output amplification, and higher efficiency compared to non-resonant operation. Examples include magnetically coupled resonance for wireless power transmission [1], and resonant filters for radio frequency communication [2]. Specific to this work, biologists have hypothesized that animals actively control their leg pendulum frequency to maintain resonance while transitioning from walking to running stride frequencies [3]. Legged robots have also leveraged this technique; for example, Raibert's hopper controlled its hopping frequency to match its body resonant frequency [4]. Multi-legged robots such as RHEX [5], ATRIAS [6], and the MIT Cheetah [7] have utilized tunable compliance in the legs to match body natural frequency to running frequency for increased speed and stability.

At smaller scales, the printed circuit MEMS (PC-MEMS) manufacturing process [8] results in flexure-based transmissions that connect an end effector (e.g. a leg or wing) to an actuator through elastic elements, resulting in a transmission resonance that is distinct from body resonance. A number of highly dynamic, insect-scale robots have been developed using PC-MEMS, including the RoboBee [9], the Harvard Ambulatory MicroRobot (HAMR) [10], and a flea-like jumping robot [11]. The size of these insect-scale robots ($\sim 100\times$ smaller characteristic length, l) results in small inertias ($\propto l^5$) and higher bandwidth ($\propto l^{-1}$), allowing them to operate at higher frequencies [12] near transmission resonance without damage to mechanical parts [13].

Harvard Microrobotics Laboratory, Harvard University, Cambridge, Massachusetts 02138, USA. Email: see http://www.micro.seas.harvard.edu

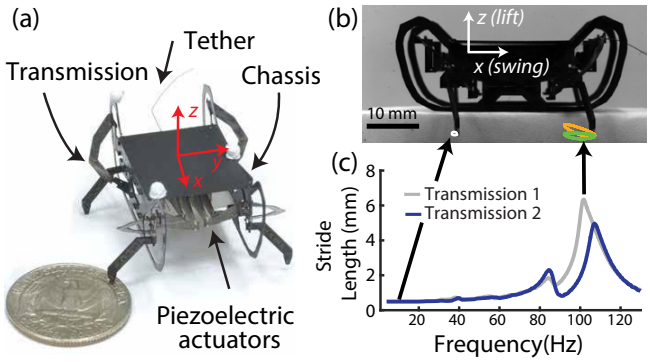

Fig. 1. (a) Labeled image of HAMR VI. (b) Side view of HAMR VI with representative open-loop, pre-resonanct (5 Hz, 40 V – white on the rear leg) and resonant (100 Hz, 40 V – orange on the front leg) leg trajectories. A closed-loop, phase-compensated, resonant trajectory is also shown in green on the front leg. (c) A plot of stride length (peak-to-peak swing displacement) versus frequency for two transmissions driven at 40 V from 1 −120 Hz.

Many insect-scale robots leverage these scaling benefits to operate at high frequencies. As a result, designs have evolved to achieve desirable transmission resonance characteristics; for example, to improve the efficiency of flapping-wing micro aerial vehicles ([14], [15]). Similarly, small legged robots such as the palm-sized X2-VelociRoACH [16] and the insect-scale HAMR have demonstrated high frequency running; however, the concept of running at transmission resonance was only briefly explored in [17]. This is largely due to difficulties in achieving desired leg trajectories and maintaining coordination between multiple legs while overcoming resonant phase lags and perturbations from high-velocity collisions with the ground.

This paper develops a high bandwidth control system for periodic leg trajectories near the resonance of HAMR's two degree-of-freedom (DOF) transmission. The controller minimizes the phase error between a reference drive signal and the estimated leg trajectory. In Section II, we describe HAMR's relevant mechanical properties, discuss the benefits of driving at transmission resonance, and explain the need for closed-loop control. We experimentally characterize transmission resonance and demonstrate that actuator phase is a sufficient proxy for leg phase in Section III. We utilize the model developed in [18] to select a desirable resonant leg trajectory in Section IV. The development of the control system is discussed in Section V, and its performance is evaluated both in air and with the presence of perturbations that approximate ground contact in Section VI.

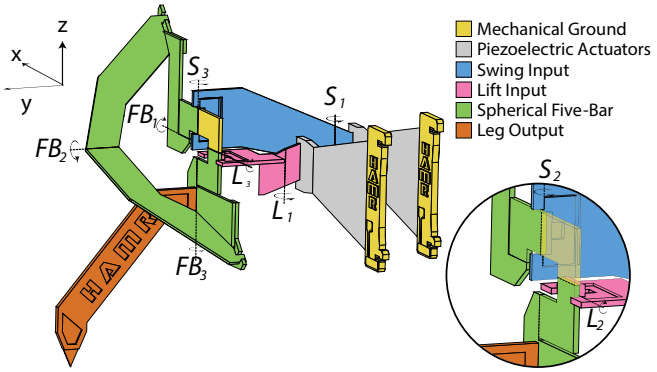

Fig. 2. Schematic of the HAMR transmission (rear right leg) with flexures labeled and subsystems color-coded .

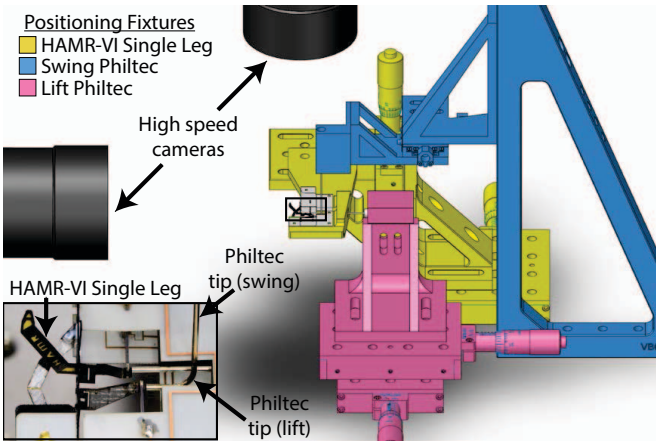

Fig. 3. SolidWorks rendering of experimental setup for resonance characterization and control system evaluation in air with positioning fixtures color coded. A HAMR-VI single leg is shown in the inset with components labeled.

II. Platform Overview

HAMR-VI, the most recent version of HAMR, is a 4.51 cm long, 1.43 g quadrupedal microrobot depicted in Figure 1a. A schematic of a single leg with labeled components is depicted in Figure 2. Each leg has two active DOFs, a lift DOF that controls leg motion in the $yz-$plane and a swing DOF that control leg motion in the $xy-$plane. The lift and swing DOFs are driven by optimal energy density piezoelectric bending actuators [19]. The transmission connects the two piezoelectric actuators to the leg. The input linkages (lift in pink and swing in blue) convert the linearized bending motion of the actuators to rotary motion and amplify the actuator displacement. The spherical five-bar (in green) maps the actuator displacements to the leg. The linkages are connected by compliant flexures (Kapton), labeled in Figure 2, which behave as rotational pin joints with an associated torsional stiffness and damping.

Each actuator is driven via an independently controlled sinusoidal voltage (Equation 1). V_b is the bias voltage (1-225 V), f_d is the drive frequency (1-120 Hz), and ϕ is the drive phase.

$$V(t) = \frac{V_b}{2}\left[1+\sin(2\pi f_d t+\phi)\right] \tag{1}$$

Setting the lift actuator drive phase to 0° and the corresponding swing actuator drive phase to -90° (an intra-leg, ϕ^{il}, phase of -90°) results in circular leg trajectories suitable for forward locomotion at pre-resonant frequencies. A representative trajectory ($f_d = 5$ Hz, $V_b = 40$ V) is depicted in white on the rear leg in Figure 1b.

Currently, HAMR-VI achieves a maximum forward velocity of approximately 0.45 m/s at a pre-resonant drive frequency 55 Hz [17]. As depicted in Figure 1c, there is a $\sim 8\times$ increase in stride length from 55 Hz to the swing resonant frequency of $\sim$100 Hz. This amplification, coupled with the increase in drive frequency, should result in faster and more efficient locomotion. For example, the robot could operate at 100 Hz with a 1/8 reduction in V_b and still maintain stride length in air. This theoretically results in a $1.4\times$ increase in speed assuming perfect ground contact with a 98% reduction in input power ($\propto V_b^2 f_d$ [19]) for driving the leg. However, actuating the transmission above 70 Hz results in a phase lag between the lift and swing drive signals and leg x and z positions, respectively. This produces leg trajectories that are not suitable for locomotion. A representative trajectory ($f_d = 100$ Hz, $V_b = 40$ V) is depicted in orange on the front leg in Figure 1b. Furthermore, variability in transmission resonance characteristics due to manufacturing and assembly errors, as evidenced by the difference between the curves in Figure 1c, makes open-loop phase compensation difficult and cumbersome as it must be done individually for each transmission. In order to operate near the swing resonant frequency, a feedback controller is needed to match the phase of the leg to a reference drive signal and command desirable leg trajectories such as the one depicted in green on the front leg in Figure 1b.

III. Resonance Characterization

Before designing a controller, the first step is to characterize the transmission's resonance. The experimental setup depicted in Figure 3 was developed to obtain an empirical understanding of the dynamics of HAMR-VI's transmission. The experiments were conducted on a single leg of HAMR-VI (inset of Figure 3). This was fixtured using a custom 3D-printed mount (Onyx, Markforged) attached to two micro-positioning stages (Thorlabs) used to center in the cameras' field of view (highlighted in yellow). The position of the leg-tip was recorded at 5 kHz by two calibrated, time-synced, high speed cameras (Phantom v7.3) positioned orthogonally. The Camera Calibration Toolbox for MATLAB was used for calibration, and the xPC target system (Mathworks) was used to sync the cameras. Vision-based tracking (Xcitex-ProAnalyst) was used to track the leg-tip in each video, and MATLAB's Camera Calibration Toolbox computed the 3D reconstruction from image correspondences. The position of each piezoelectric actuator was measured at 10 kHz using a time-synced one dimensional fiberoptic displacement sensor (Philtec-D21). Each sensor was fixtured with two micro-positioning stages and custom brackets to enable precise placement relative to the actuators (lift in pink and swing in blue).

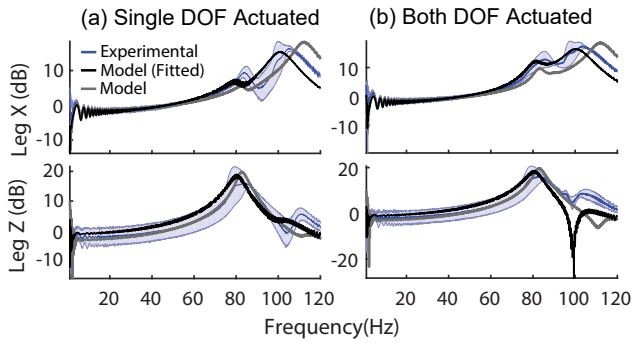

Fig. 4. Frequency response HAMR's transmission the actuator of interest driven (a), and with both actuators driven (b). The dashed blue line represents the mean (n=4) experimental data, and the light blue shaded area is a ± one standard deviation window. The light gray line represents the model response, and the black line is model response after fitting to the experimental data (Section IV-A).

Two different single leg transmissions were tested to observe the effects of variations in material properties and manufacturing imperfections. The lift and swing actuators were driven individually (with the other fixed at $^1/_2V_b$) and then simultaneously, with $\phi^{\text{il}} = -90°$, by an eight second long chirp signal between 1-120 Hz. A bias voltage of 40 V was chosen for each condition – lift DOF actuated, swing DOF actuated and both DOFs actuated – and tests were repeated twice for a total of twelve trials (six per transmission tested). Higher bias voltages were not tested as they resulted in collisions between the leg and the chassis.

The blue traces in Figure 4 display the experimental frequency response of the transmission. The top row displays frequency response in the swing (x) direction, and the bottom row displays the frequency response in the lift (z) direction. Figure 4a shows the frequency response with only the DOF of interest driven, and Figure 4b shows the frequency response with both DOFs actuated. The two DOFs have separate resonances, with the lift resonance at 81.3 ± 3.8 Hz (n=4), and the swing resonance at 103.0 ± 3.33 Hz (n=4). Both of these peaks have a high quality factor, with $Q_{\text{lift}} = 10.3 \pm 3.3$ (n=4) for the lift, and $Q_{\text{swing}} = 9.6 \pm 1.5$ (n=4) for the swing. This indicates a significant increase in $z-$amplitude at the lift resonance and $x-$amplitude at the swing resonance. Furthermore, Figure 4b shows that the two DOFs are coupled at resonance, as the frequency response in the x direction has a smaller secondary peak at the lift resonant frequency, and the frequency response in the z direction has a trough near the swing resonant frequency.

A. Sensor Selection

Characterizing the transmission resonance also assists in identifying a sensor strategy to estimate leg phase. Options include measuring the position of the leg tip, the deformation of the joints, the deflection of the piezoelectric actuators, or a combination thereof. Measuring actuator deflection is the simplest in terms of integration on-board HAMR as the actuators are closest to mechanical ground for ease of access and wiring. However, it is not clear if actuator phase is an adequate proxy for leg phase as parasitic compliance was observed in a previous iteration of HAMR [20].

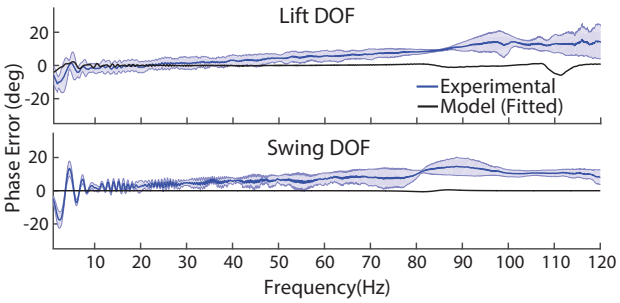

Fig. 5. Phase between leg position and actuator position for lift DOF (top) and swing DOF (bottom) with both actuators driven. Average experimental data (n=4) is shown (blue) with a ± one standard deviation window in light blue, and the model response is shown in black.

We used the chirp response with both DOFs actuated (Section III) to compute the phase difference between the actuator deflection and leg position for the range of operating frequencies (1-120 Hz). We assume that the lift actuator control leg z position, and the swing actuator controls the leg x position. The phase between the actuator deflection and leg position is calculated by taking the difference between the phase angle of the Hilbert transform of the two time traces. The resulting phase difference was filtered with a centered moving average filter to reduce ringing. The raw actuator position data was also filtered using an acausal second order low pass Butterworth filter with a cutoff frequency of 500 Hz. Figure 5 displays the mean phase difference between the actuators and leg with both actuators driven in blue, and with the phase difference as predicted by the fitted model (Section IV-A) in black. This analysis indicates that, though coupling between the two DOFs is visible at resonance, actuator phase is a good proxy for leg phase with RMS phase error of 8.8 ± 0.8° (n=4) for the lift DOF and 9.0 ± 1.0 ° (n=4) for the swing DOF.

IV. Nonlinear Modeling

Having experimentally characterized the transmission's resonance, the nonlinear, numerical model developed in [18] was used to verify the experimental data, select a desirable resonant leg trajectory, and determine corresponding open-loop control inputs. This transmission model has four states (the positions and velocities of the two actuators), two control inputs (the drive voltage for each actuator), and two outputs (leg position in the x and z directions). Simplification to this general model, namely, analyzing the transmission as two single-input, single-output systems with the lift actuator controlling the $z-$position of the leg, and the swing actuator controlling the $x-$position of the leg have been explored in [17] and [18]. However, the coupling described in Section III indicates that the multi-input, multi-output system must be considered near resonance.

A. Model Fitting

The simulated transmission was also driven by an eight second long linear chirp between 1-120 Hz to verify the experimental data. The model frequency response was determined using the same technique described in Section III, and is plotted in gray in Figure 4. The model matches the

experimental frequency response well at low frequencies (1-40 Hz), and captures the shape of the experimental frequency response correctly near resonance. However, the resonant frequency and the quality factor of the model response does not match the data. We hypothesize this is due to three factors: (1) an incomplete model for the flexure stiffness and damping at large angles and high frequencies, (2) assembly imperfections leading to a non-zero neutral angle for the flexure, and (3) manufacturing imperfections leading to reduced actuator performance.

As such, we use a nonlinear least squares regression to fit the model chirp response to the four experimental chirp responses. The least squares regression minimizes the squared modified euclidean distance between the model-predicted and experimentally measured leg positions (Equation 2).

$$F = (x^{\text{exp}} - x^{\text{mp}})^2 + \frac{1}{2}(y^{\text{exp}} - y^{\text{mp}})^2 + \frac{1}{2}(z^{\text{exp}} - z^{\text{mp}})^2 \quad (2)$$

Here, x, y and z are the Cartesian coordinates of the leg position, superscripts 'mp' and 'exp' stand for model-predicted and experimental, and the factor of $1/2$ multiplies squared position error in y and z because both are determined by the lift DOF. The decision variables were chosen to address the aforementioned model limitations, and include flexure stiffness coefficients, damping coefficients, neutral angles ($\in [-20^o, 20^o]$), and two actuator "efficiency" coefficients ($\in [0,1]$). The linkage geometries, masses and inertias were assumed to be correct and are not included in the optimization.

The time traces of the fitted model's chirp response matches the average experimental chirp response closely when both DOFs are driven (frequency response shown in Figure 4b and phase shown in Figure 8), with an RMS error between model predicted and experimental leg position of 325 $\pm$ 151 µm (n=4) for the lift and 328 $\pm$ 78 µm (n=4) for the swing. Furthermore, time trace of the fitted model's chirp response also closely matches the average experimental chirp response in the actuated direction for the lift DOF (frequency response shown in bottom plot of Figure 4a) with a RMS position error of 347 $\pm$ 197 µm (n=4), and for the swing DOF (frequency response shown intop plot of Figure 4a) with a RMS position error of 380 $\pm$ 98 µm (n=4).

After the model has been experimentally verified, it is utilized to select an appropriate resonant trajectory (Section IV-B) and to determine feed-forward control inputs (Section V).

B. Trajectory Selection

Baisch et al. showed that maintaining an intra-leg phasing of -90° at pre-resonant frequencies results in circular leg trajectories for rapid locomotion [17]. As illustrated in Figure 1, phase lag between the leg and drive signals at resonance generate skewed leg trajectories that are hypothesized to result in reduced speeds. In this section, we use the model to explore different leg trajectories near resonance. Intuitively, an elliptical leg trajectory that is close to flat (major axis aligned with the $x-$direction) will exhibit a large increase in stride length compared to pre-resonant trajectories, without large perturbations from vertical motion due to the lift DOF. This, however, is a heuristic approach, and the choice of trajectory shape is a subject of future work.

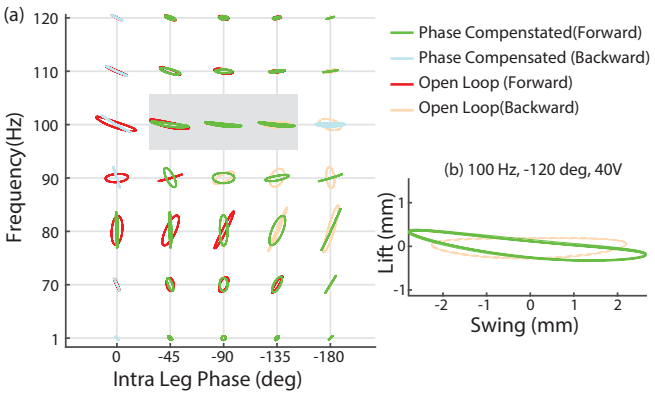

Fig. 6. (a) Parameter sweep over frequencies from 1-120 Hz and intra-leg phases from 0 to -180°. An operating regime around the swing resonance of 100 Hz with an intra-leg phase of -45 to -135° was selected and is shaded in gray. A representative trajectory is shown in (b).

As the lift and swing DOFs are driven by sinusoidal signals, the appropriate trajectory is selected by performing parameter sweeps over frequencies from $1-120$ Hz and phases from -180° to 180° at a drive voltage of 40 V. Other voltages are not considered as it is known that trajectory amplitude is proportional to voltage. The results for a coarse sweep are shown in Figure 6a, with positive intra-leg phases omitted as the results mirror what is shown. The open loop trajectories represent instances when the intra-leg phase between the lift and swing DOFs is determined by the natural dynamics of the system. The phase-compensated trajectories are generated when the drive signals are appropriately shifted to force the phase between the lift and swing DOFs to maintain the value indicated on the x-axis.

Based on these parameter sweeps, it seems that operating near the swing resonant frequency ($\sim$100 Hz) at intra-leg phases near -90° with phase compensation results in ideal elliptical leg trajectories with the largest stride lengths for a given bias voltage. A representative trajectory ($f_d = 100$ Hz, $V_b = 40$ V, $\phi^{\text{il}} =$ -120°) is shown in 6b, and has an approximately 5$\times$ increase in stride length from the previously used 65 Hz leg trajectory when driven with a bias voltage of 40 V.

V. Control System Design

Results from previous work by Baisch et al. and the model developed in Section IV indicate that the relative phase between the lift (leg z position) and swing (leg x position) determines the shape of the leg trajectory. Furthermore, since the system is periodic, actuator position can be represented by an amplitude and a phase. As such, we design a controller that alters actuator phase to achieve a desired leg trajectory (Figure 7). Simple architectures are used for the estimator (recursive least squares - RLS) and the controller (proportional-integral-derivative - PID) to keep computational costs low as this system will eventually be implemented on-board HAMR.

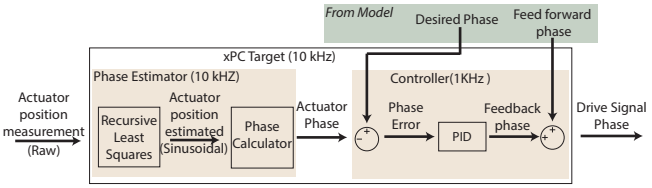

Fig. 7. Block diagram of the control system. Sensor measurements are read in at 10 kHz and are used to compute a phase estimate. Control commands are computed at 1 kHz and are sent to the HAMR-VI single leg.

A. Estimator Design

In order to perform phase control with noisy sensor data, an estimator was designed to obtain an accurate phase estimate. Since the actuator position is well represented by a sinusoid at the frequency of the drive signal, a pure sinusoid can be fit in real time to the noisy sensor measurements using the RLS algorithm. This pure sinusoid can then be used to obtain a closed form phase estimate at each time step. The form of the fitted sinusoid is given by Equation (3).

$$\hat{y}(t) = C_1 \sin(2\pi f_d t) + C_2 \cos(2\pi f_d t) + C_3 \tag{3}$$

Here f_d is the known drive frequency and t is time. The parameters to be estimated are $\{C_1, C_2, C_3\}$, the regressors are $\{\sin(2\pi f_d t), \cos(2\pi f_d t), 1\}$, and the output being fitted to is the raw sensor measurement, $y(t)$. The parameters are estimated at each step by solving the linear system given by Equation (4) using RLS with a frequency dependent exponential forgetting factor $\alpha(f_d)$ to allow the estimator to respond to changes in phase resulting from control commands discussed in Section V-B.

$$y(t) = \begin{bmatrix} \sin(2\pi f_d t), & \cos(2\pi f_d t), & 1 \end{bmatrix} \begin{bmatrix} C_1 \\ C_2 \\ C_3 \end{bmatrix} \tag{4}$$

A separate estimator is implemented for the lift and swing actuators on the xPC Target at 10 kHz using Simulink's RLS estimator block; thus, six parameters are estimated: $\{C_1^{\mathrm{l}}, C_2^{\mathrm{l}}, C_3^{\mathrm{l}}, C_1^{\mathrm{s}}, C_2^{\mathrm{s}}, C_3^{\mathrm{s}}\}$. The superscripts l and s represent the lift and swing DOF, respectively. The forgetting factors for both DOFs are set as a function of the drive frequency and are proortional to the equation given in [21]. The parameters $C_1^{\mathrm{l,s}}$ and $C_2^{\mathrm{l,s}}$ are initialized to zero, the covariance matrices are initialized to the identity, and $C_3^{\mathrm{l,s}}$ is set to the mean of the lift and swing sensor readings, respectively. The phase of the lift and swing actuators are calculated from the estimated signals as $\hat{\phi}^{\mathrm{l}}(t) = \arctan(C_2^{\mathrm{l}}/C_1^{\mathrm{l}})$ and $\hat{\phi}^{\mathrm{s}}(t) = \arctan(C_2^{\mathrm{s}}/C_1^{\mathrm{s}})$, respectively.

B. Controller Design

Two separate PID controllers with a model-based feed forward term were implemented at 1 kHz (to allow the estimator to settle) on the xPC target system to separately control lift and swing phase. The controller begins to command phase one cycle after the estimator has been started to allow for the phase estimates to converge. The controller minimizes the error between the desired leg phase, $\phi_{\mathrm{r}}^{\mathrm{l,s}}$, and the estimated actuator phase, $\hat{\phi}^{\mathrm{l,s}}$. based on the control law given by Equation (5).

$$\begin{aligned} \phi_{\mathrm{d}}^{\mathrm{l,s}} = \phi_{\mathrm{r}}^{\mathrm{l,s}} + \phi_{\mathrm{ff}}^{\mathrm{l,s}} + K_P^{\mathrm{l,s}}(\phi_{\mathrm{r}}^{\mathrm{l,s}} - \hat{\phi}^{\mathrm{l,s}}) \ \ldots \\ + K_I^{\mathrm{l,s}} \int (\phi_{\mathrm{r}}^{\mathrm{l,s}} - \hat{\phi}^{\mathrm{l,s}}) \mathrm{dt} + K_D^{\mathrm{l,s}} \frac{\mathrm{d}}{\mathrm{dt}} (\phi_{\mathrm{r}}^{\mathrm{l,s}} - \hat{\phi}^{\mathrm{l,s}}) \end{aligned} \tag{5}$$

Here $\phi_{\mathrm{ff}}^{\mathrm{l,s}}$ is the model-based feed forward phase, $\phi_{\mathrm{d}}^{\mathrm{l,s}}$ is the commanded drive phase, K_P, K_I, and K_D are the controller gains, and the superscripts 'l' and 's' represent the lift and swing DOF, respectively. The gains are manually tuned for an operating condition (f_d and ϕ^{il}), and the feed forward phases for the lift and swing are calculated from a lookup table using linear interpolation between the two nearest operating conditions. The lookup table has been pre-computed for frequencies between 1-120 Hz and intra leg phases of -45 to -135° at intervals of 15° using the model. An example for an open-loop intra-leg phase of -90° is depicted in Figure 8, and compared against experimental data taken from the four transmissions. The feed-forward phase is simply the negative of the phase lag depicted in Figure 8.

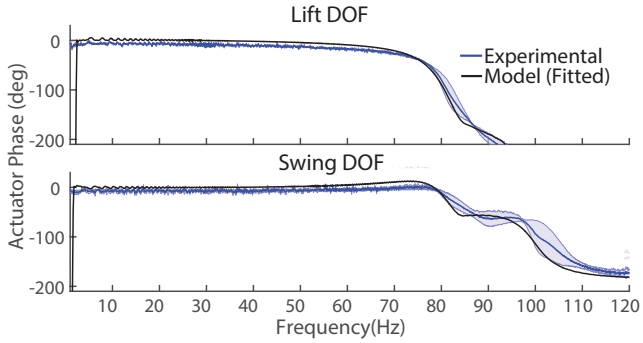

Fig. 8. Model predicted actuator phase (black) compared against mean (n=4) experimental actuator phase (blue – Section III) with a ± one standard window in light blue for the lift DOF (top) and swing DOF (bottom). Phase computed as in Section III-A. The feed-forward phase used for the controller is the negative of model predicted actuator phase.

VI. Results

The performance of the estimator was evaluated over the range of operating frequencies to demonstrate its rapid convergence, and the control of the resonant trajectory selected in Section IV-B (f_d = 100 Hz, V_b = 40 V, and ϕ^{il} =-120°) is demonstrated in air and in the presence of ground contact (see accompanying video).

A. Estimator Results

The performance of the estimator was evaluated using the experimental set-up described in Section III for a variety of frequencies: 10, 80, 90, 100, and 110 Hz. Two tests were taken at each frequency. Independent of tested frequency, the estimator converges to within ± 5° of the steady state open-loop phase estimate in 0.36 ± 0.1 cycles (n = 10) for the the lift DOF, and in 0.65 ± 0.15 cycles (n = 10) for the swing DOF. Figure 9 shows the estimator performance for the 100 Hz resonant trajectory (swing DOF). The raw sensor data (gray pluses) and best-fit signal (black) during open-loop operation is shown in the top plot of Figure 9a. The

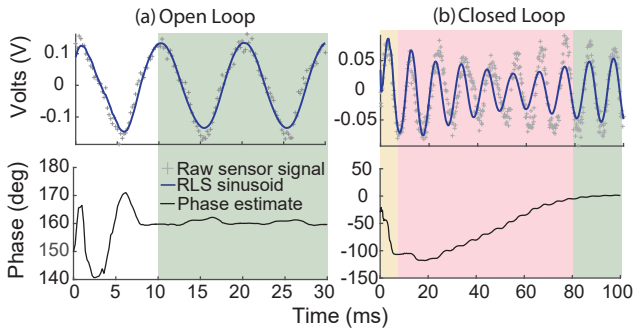

Fig. 9. (a) Estimator performance for the resonant trajectory (100 Hz) in the open-loop case (swing DOF). The estimated phase converges to the steady state phase (green) in less than one cycle. (b) Estimator performance for the same trial when the controller is active. The controller is not active for the first cycle (tan), the estimate lags slightly behind the raw data during the transient region (red), but recovers near steady-state.

corresponding phase estimate is shown in the bottom plot of Figure 9a, which converges in approximately 8 ms (0.80 cycles) to the steady state estimate (highlighted in green).

Figure 9b shows the same data for a closed-loop trial at the resonant trajectory. The estimated signal lags slightly behind the raw sensor data during the transient region when the controller is changing the phase (highlighted in red), but catches up due to the exponential forgetting factor. The estimator matches the raw data closely during steady state (highlighted in green). Though decreasing the forgetting factor would reduce lag during the transient region, it would allow sensor noise to corrupt the estimated sinusoid.

B. Controller Results

The controller was tested in two transmissions at the resonant trajectory selected in Section IV-B, both in air and with perturbations that simulate ground contact. The tests in air were performed using the experimental set-up shown in Figure 3. The tests with ground contact were performed on a slightly modified experimental set-up show in Figure 10. The HAMR-VI single leg was flipped so that the leg was pointed downwards, and the positioning fixtures (Figure 3) were reconfigured accordingly. A running surface (cardstock glued to a glass slide) was positioned so that the leg rested on it in the neutral position. Rotating the mount obscured the overhead camera; therefore, the leg position was tracked by a single (manually calibrated) high speed camera (Phantom v7.3) orthogonal to the lift-swing (xz) plane.

The control gains were tuned manually for the in air and ground contact trials, and for each transmission tested (Table I). Derivative gains (K_D) were small (or omitted) as they caused instability. The model-based feed-forward phase is 180° for the lift, and 122° for the swing.

TABLE I

CONTROLLER GAINS

Gain	Lift		Swing	
	Ground*	Air*	Ground*	Air*
K_P	2.0 (0.8)	2.0 (2.0)	1.3 (1.5)	2.4 (2.4)
K_I	85 (55)	100 (100)	55 (75)	100 (100)
K_D	0 (0)	0.03 (0)	0.01 (0)	0.04 (0)

* Control gains are reported as Transmission 1 (Transmission 2)

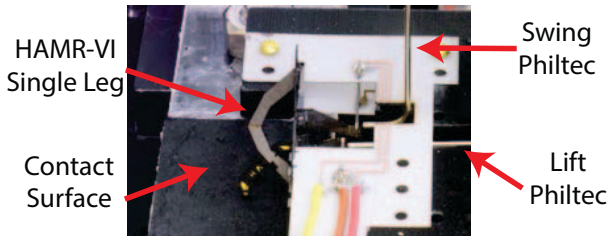

Fig. 10. Experimental setup for control system evaluation under perturbations from ground contact with components labeled.

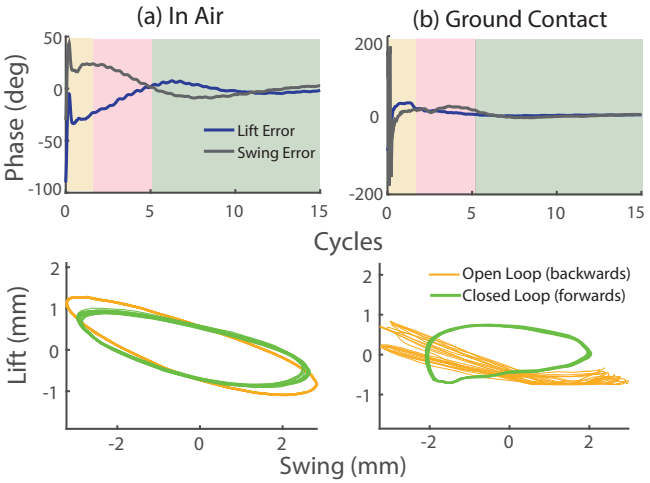

Fig. 11. Controller performance for resonant trajectories (a) in air (f_d = 100 Hz, ϕ^{il} =-120°, V_b = 40 V), and (b) with ground contact (f_d = 100 Hz, ϕ^{il} =-120°, V_b = 80 V). Open-loop (orange) and controlled (green) leg trajectories shown in bottom figures, with corresponding lift (blue) and swing (gray) phase errors in top figures. The response is divided into three regions, no control (tan), transient (pink) and steady state (green). The same is shown in (b) with perturbations from ground contact.

1) In Air: Four tests, two with each transmission were performed. The lift and swing phase errors settle to within ± 10° of zero in 0.053 ± 0.02 (n=4) seconds (5.3 ± 2.4 cycles) and 0.043 ± 0.01 (n=4) seconds (4.3 ± 0.5 cycles), respectively. The shape of the open-loop (orange) and closed-loop (green) leg trajectories for a representative trial without ground contact are shown in the bottom plot of Figure 11a. It is important to note that the open-loop test results in backwards leg trajectories, and the controller is needed to restore a forward trajectory with similar shape. The corresponding phase errors for the lift (blue) and swing (gray) DOF are shown in the top plot of Figure 11a. The shaded regions have the same meaning as discussed in Section VI-A. The trajectories are similar to the model predictions (Section IV-B), and they exhibit a large ∼5 mm stride length.

2) On Ground: Four tests, two with each transmission were performed. The bias voltage was increased to 80 V to compensate for energy lost to ground contact, resulting in similar stride lengths as the in air case. The lift and swing phase errors settle to within ± 10° of zero in 0.035 ± 0.01 seconds (n=4) (3.5 ± 0.6 cycles) and 0.47 ± 0.01 seconds (n=4) (4.7 ± 0.6 cycles), respectively. A representative trial with ground contact is shown in Figure 11b. The open-loop (orange) leg trajectory is moving backwards, and the shape is unsuitable for locomotion. The closed-loop (green) leg trajectory restores forward motion, and results in a leg

trajectory that is suitable for locomotion according to the criteria discussed in Section IV-B. The corresponding phase errors for the lift and swing DOFs are shown in the bottom plot of Figure 11b. Since minimizing actuator phase error results in a trajectory similar to those commanded in air, actuator position is still a good proxy for leg position even when contact with the ground is being made.

C. Energy Considerations

A primary motivation for operating at resonance is to minimize energy consumption. In air, HAMR achieves a 5 mm stride length at a drive frequency of 100 Hz and a bias voltage of 40 V. With ground contact, the voltage must be increased to 80 V to achieve a similar stride length ($\sim$4 mm). Based on the model (Section IV), a bias voltage of 140 V is needed to achieve 5 mm of stride in air at the operating frequency (65 Hz) that has previously resulted in HAMR's fastest locomotion. Thus, running at resonance results in theoretical power reductions of 87% (in air) and 50% (with ground contact) while maintaining stride length. This should enable a significant reduction in power consumption for autonomous operation.

VII. Conclusions and Future Work

In this paper, we experimentally characterized the resonance of HAMR's two DOF transmission, and utilized this data to determine that actuator phase is an adequate proxy for leg phase. A non-linear dynamic model was fit to the experimental data and was used to select open-loop resonant leg trajectories and define feed-forward control inputs. An off-board phase controller was designed to command leg trajectories at resonance, and was shown to converge quickly (in approximately five cycles) to the desired trajectory both in air and under cyclic perturbations that approximate ground contact. This phase control system is a first step towards leveraging the large increase in stride length at transmission resonance for faster and more efficient locomotion.

In the future, we will integrate this controller and estimator with on-board sensor being developed concurrently, and use it in a hierarchical control structure to run HAMR at resonance. We can also improve controller performance by using the dynamic model discussed to: (1) find a transformation (e.g modal coordinates) to decouple two the DOFs at resonance and determine more intelligent control inputs; and (2) apply trajectory optimization techniques to determine leg trajectories for running at resonance that, for example, maximize speed or minimize cost of transport

Finally, in addition to is applications for HAMR, phase control for resonant operation can be applied to other robots that are periodically actuated and utilize elastic transmissions such as the RoboBee or DASH [22].

VIII. Acknowledgments

This work is partially funded by the Wyss Institute for Biologically Inspired Engineering and the National Defense Science and Engineering Graduate Fellowship. In addition, the prototypes were enabled by equipment supported by the ARO DURIP program (award #W911NF-13-1-0311).

References

[1] M. Karpelson, B. H. Waters, B. Goldberg, B. Mahoney, O. Ozcan, A. Baisch, P.-M. Meyitang, J. R. Smith, and R. J. Wood, "A wirelessly powered, biologically inspired ambulatory microrobot," in *IEEE Intl. Conf. on Robotics and Automation*. IEEE, 2014, pp. 2384–2391.

[2] M. Makimoto and S. Yamashita, *Microwave resonators and filters for wireless communication: theory, design and application*. Springer Science & Business Media, 2013, vol. 4.

[3] B. K. Ahlborn and R. W. Blake, "Walking and running at resonance," *Zoology*, vol. 105, no. 2, pp. 165–174, 2002.

[4] M. Raibert, M. Chepponis, and H. Brown, "Running on four legs as though they were one," *IEEE Journal on Robotics and Automation*, vol. 2, no. 2, pp. 70–82, 1986.

[5] K. C. Galloway, J. E. Clark, and D. E. Koditschek, "Design of a tunable stiffness composite leg for dynamic locomotion," in *ASME 2009 International Design Engineering Technical Conferences and Computers and Information in Engineering Conference*. American Society of Mechanical Engineers, 2009, pp. 215–222.

[6] J. W. Hurst, J. E. Chestnutt, and A. A. Rizzi, "An actuator with physically variable stiffness for highly dynamic legged locomotion," in *IEEE Intl. Conf. on Robotics and Automation*, vol. 5. IEEE, 2004, pp. 4662–4667.

[7] D. J. Hyun, S. Seok, J. Lee, and S. Kim, "High speed trot-running: Implementation of a hierarchical controller using proprioceptive impedance control on the MIT cheetah," *The International Journal of Robotics Research*, vol. 33, no. 11, pp. 1417–1445, 2014.

[8] J. P. Whitney, P. S. Sreetharan, K. Y. Ma, and R. J. Wood, "Pop-up book MEMS," *Journal of Micromechanics and Microengineering*, vol. 21, no. 11, p. 115021, 2011.

[9] K. Y. Ma, S. M. Felton, and R. J. Wood, "Design, fabrication, and modeling of the split actuator microrobotic bee," in *IEEE/RSJ Intl. Conf. on Intelligent Robots and Systems*. IEEE, 2012, pp. 1133–1140.

[10] A. T. Baisch, "Design, manufacturing, and locomotion studies of ambulatory micro-robots," Ph.D. dissertation, John A Paulson School of Engineering and Applied Sciences, Harvard University, 2013.

[11] J.-S. Koh, S.-P. Jung, M. Noh, S.-W. Kim, and K.-J. Cho, "Flea inspired catapult mechanism with active energy storage and release for small scale jumping robot," in *IEEE Intl. Conf. on Robotics and Automation*. IEEE, 2013, pp. 26–31.

[12] W. S. Trimmer, "Microrobots and micromechanical systems," *Sensors and Actuators*, vol. 19, no. 3, pp. 267–287, 1989.

[13] J. B. Haldane, "On being the right size," *Harpers Magazine*, vol. 152, pp. 424–427, 1926.

[14] N. T. Jafferis, M. A. Graule, and R. J. Wood, "Non-linear resonance modeling and system design improvements for underactuated flapping-wing vehicles," in *IEEE Intl. Conf. on Robotics and Automation*. IEEE, 2016, pp. 3234–3241.

[15] S. S. Baek, K. Y. Ma, and R. S. Fearing, "Efficient resonant drive of flapping-wing robots," in *IEEE/RSJ Intl. Conf. on Intelligent Robots and Systems*. IEEE, 2009, pp. 2854–2860.

[16] D. W. Haldane and R. S. Fearing, "Running beyond the bio-inspired regime," in *2015 IEEE International Conference on Robotics and Automation (ICRA)*. IEEE, 2015, pp. 4539–4546.

[17] A. T. Baisch, O. Ozcan, B. Goldberg, D. Ithier, and R. J. Wood, "High speed locomotion for a quadrupedal microrobot," *The International Journal of Robotics Research*, pp. 1063–1082, 2014.

[18] N. Doshi, B. Goldberg, R. Sahai, N. Jafferis, D. Aukes, and R. J. Wood, "Model driven design for flexure-based microrobots," in *IEEE/RSJ Intl. Conf. on Intelligent Robots and Systems*. IEEE, 2015, pp. 4119–4126.

[19] N. T. Jafferis, M. J. Smith, and R. J. Wood, "Design and manufacturing rules for maximizing the performance of polycrystalline piezoelectric bending actuators," *Smart Materials and Structures*, vol. 24, no. 6, p. 065023, 2015.

[20] O. Ozcan, A. T. Baisch, D. Ithier, and R. J. Wood, "Powertrain selection for a biologically-inspired miniature quadruped robot," in *IEEE Intl. Conf. on Robotics and Automation*. IEEE, 2014, pp. 2398–2405.

[21] B. Lindoff, "On the optimal choice of the forgetting factor in the recursive least squares estimator," Department of Mathematical Statistics, Lund Institute of Technology, Tech. Rep., 10 1997.

[22] P. Birkmeyer, K. Peterson, and R. S. Fearing, "Dash: A dynamic 16g hexapedal robot," in *IEEE/RSJ Intl. Conf. on Intelligent Robots and Systems*. IEEE, 2009, pp. 2683–2689.